Supplementary Material

Cruise	Longitudinal coverage	Latitudinal coverage	Period	DOI
M158	[-44.24 ; 11.36]	[-6.45 ; 0]	26/09/2019-22/10/2019	https://doi.pangaea.de/10.1594/PANGAEA.952354
M181	[-44.25 ; 10.96]	[-6 ; 0]	27/04/2022-20/05/2022	https://doi.pangaea.de/10.1594/PANGAEA.952520
MSM117	[-37.62 ; -23.11]	[-11.50 ; 4.98]	10/05/2023-3/06/2023	https://zenodo.org/records/18637164
M147	[-47.6 ; -46.44]	[1.91 ; -3.95]	1/05/2018-4/05/2018	https://doi.org/10.1594/PANGAEA.941355
M174	[-56.72 ; -30.64]	[2.52 ; 15.03]	16/04/2021-13/05/2021	https://doi.org/10.1594/PANGAEA.942346
M159	[-35.01 ; -32]	[-11.5 ; 6]	2/11/2019-13/11/2019	https://doi.pangaea.de/10.1594/PANGAEA.952516

Table 1: Spatial and temporal coverage of the cruises reported in this study. The table lists each cruise, its dates, and the geographic area sampled.

Region	M158	M181
East (5°E to 15°W)*	496±181	319±105
Center (15°W to 30°W)	388±105	339±90
West (30°W to end)*	344±76	231±85

Table 2: Mean integrated primary production (mg m^{-2} d^{-1}) for M158 and M181 based on regions. Values are reported as mean ± standard deviation. Asterisks (*) indicate statistically significant differences between regions.

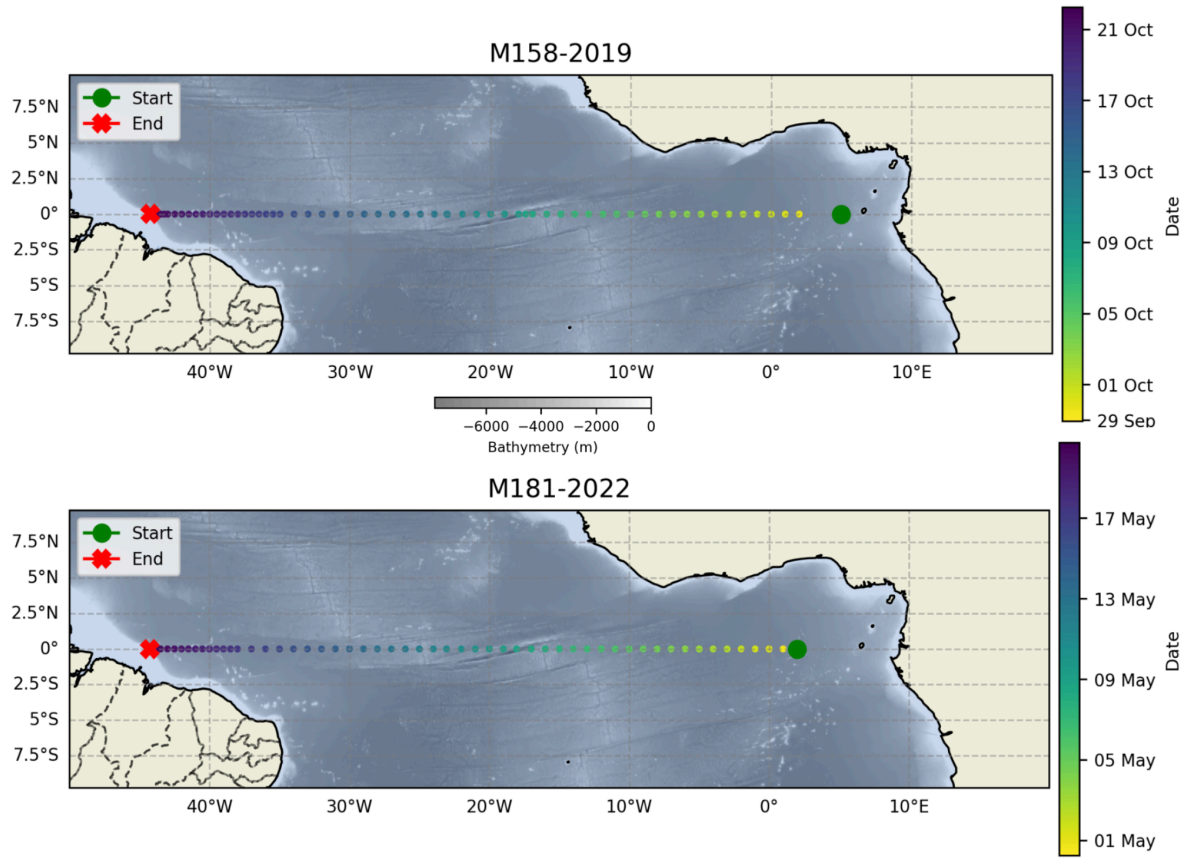

Fig. S1 | Cruise trajectory. Locations of CTD stations during the M158 and M181 cruises along the Equatorial Atlantic. Stations form longitudinal transects conducted from east to west across the equator. The green dot shows the starting position of the cruise and the red cross the ending.

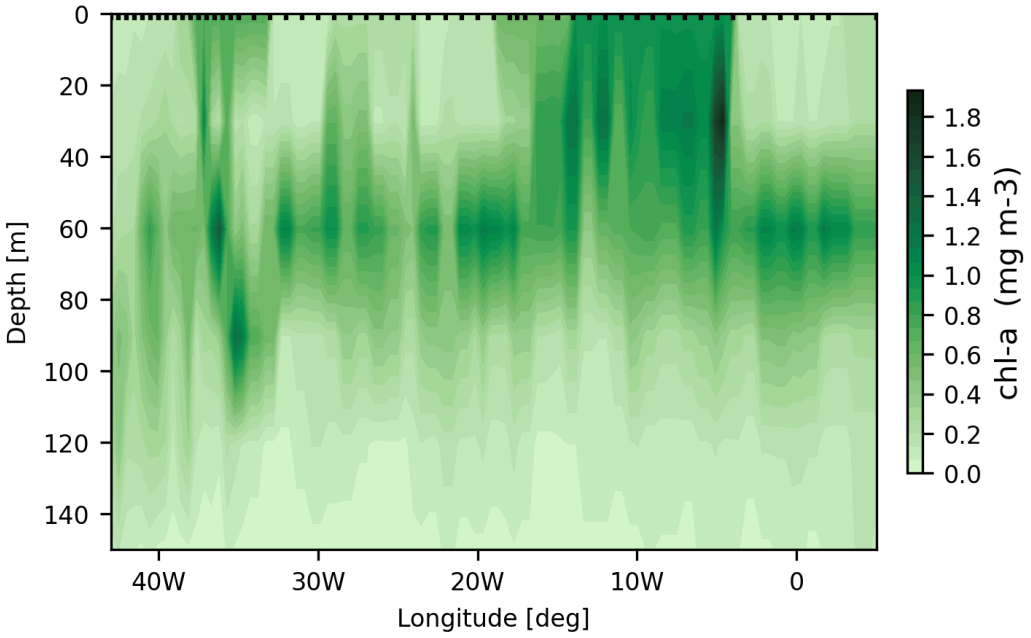

Fig. S2 | Vertical profiles of relative chlorophyll-*a* fluorescence measured by the CTD-mounted fluorometer during the M158 cruise. Apparent smoothing reflects interpolation onto a regular grid and

contour rendering; no additional spatial smoothing was applied. Fluorescence values are shown in instrument units and are used to illustrate relative vertical and spatial variability in phytoplankton biomass. The fluorometer was not calibrated against extracted chlorophyll-*a* concentrations; absolute chlorophyll-*a* values should therefore be interpreted qualitatively. Vertical profiles of chl-a measured by in situ fluorometry during the M158 cruise illustrate spatial variability in phytoplankton biomass across stations. Elevated chlorophyll-*a* concentrations were observed throughout the mixed layer between 20°W and 10°W, with additional subsurface maxima at 25–30°W and a distinct double subsurface peak near 39°W. Due to a sensor malfunction during the M181 cruise, in situ chlorophyll-*a* profiles could not be obtained for the spring period.

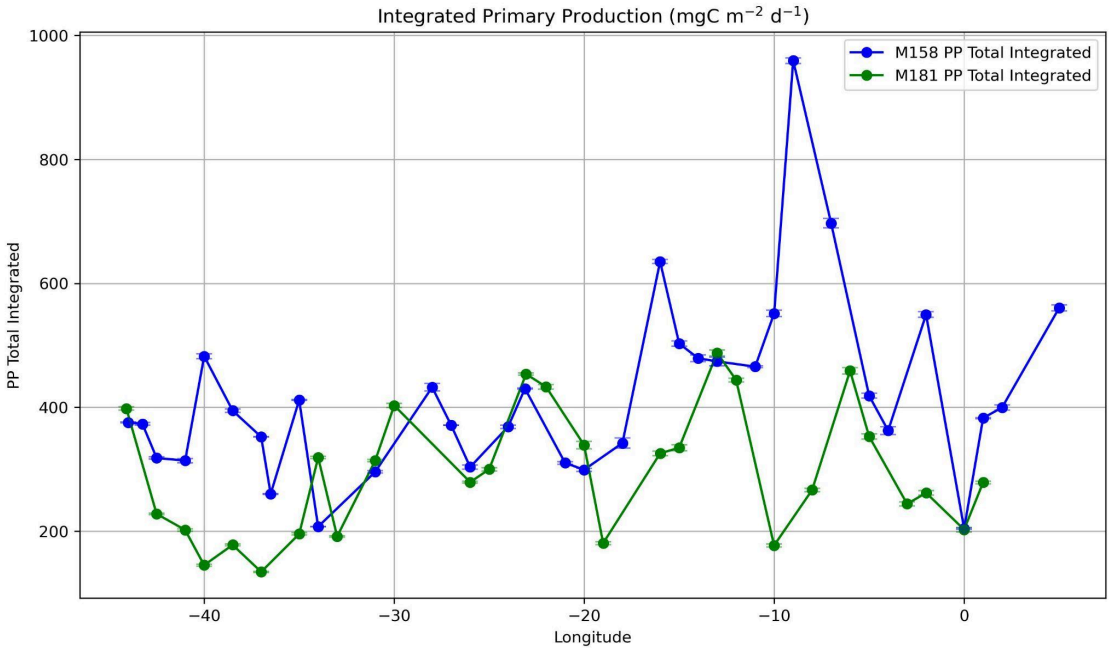

Fig. S3 | Vertically integrated primary production (mg C m^{-2} d^{-1}) for M158 and M181. Primary production integrated from the surface to the deep chlorophyll maximum (DCM) at all stations sampled during the M158 (fall 2019) and M181 (spring 2022) cruises. Values were calculated using trapezoidal integration of in situ primary production profiles from surface to the deep chlorophyll maximum (30-110 m depending on the region). M158 exhibits elevated primary production in the eastern basin near 10°W, with additional peaks near 15°W and 40°W compared to M181. In contrast, M181 shows consistently low primary productivity in the west, indicating a basin-wide relatively lower-productivity regime during the cruise period compared to M158. Error bars represent measurement uncertainty and are small. Seasonal differences between fall and spring were statistically significant (*p value < 0.05)* in the eastern and western regions.

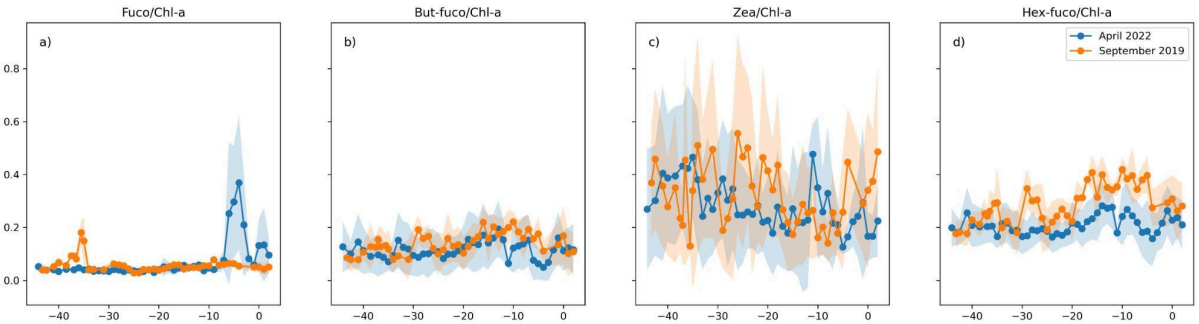

Fig. S4 | Relative phytoplankton group contributions inferred from diagnostic pigment ratios during the a–d) M158 and e–h) M181 cruises. Ratios of diagnostic pigments to total chlorophyll-*a* are shown. Zeaxanthin (Zea/Chl-a) indicates contributions from cyanobacteria and prochlorophytes; hexanoyloxyfucoxanthin

(Hex-fuco/Chl-a) and butanoyloxyfucoxanthin (But-fuco/Chl-a) reflect contributions from chromophyte nanoflagellates; and fucoxanthin (Fuco/Chl-a) reflects contributions from diatoms.

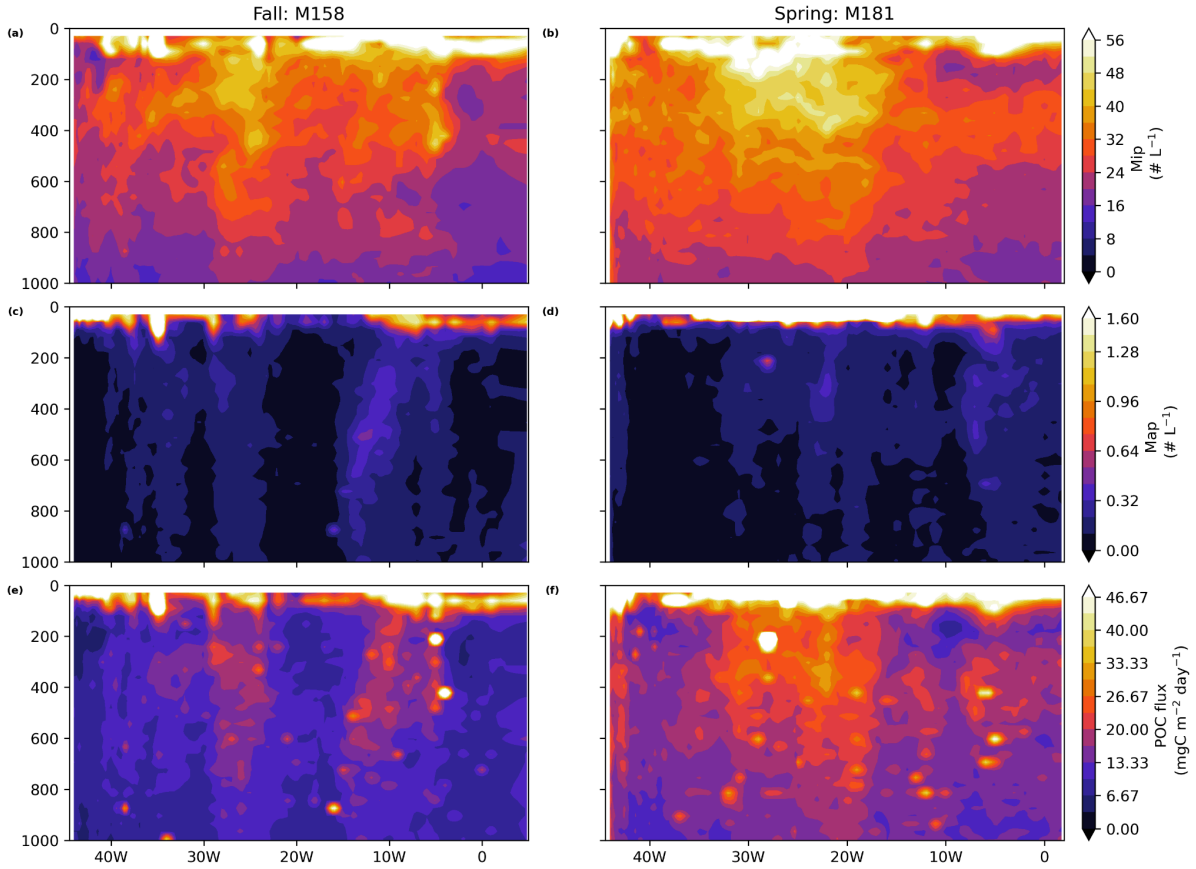

Fig. S5 | Particle abundance and carbon flux during M158 and M181 in the top 1000m of the water column. (a, b) MiP abundance (# L^{-1}), (c, d) Map abundance (# L^{-1}), and (e, f) POC flux (mg C m^{-2} day^{-1}) measured during the two trans-Atlantic crossings, M158 (left panels) and M181 (right panels).

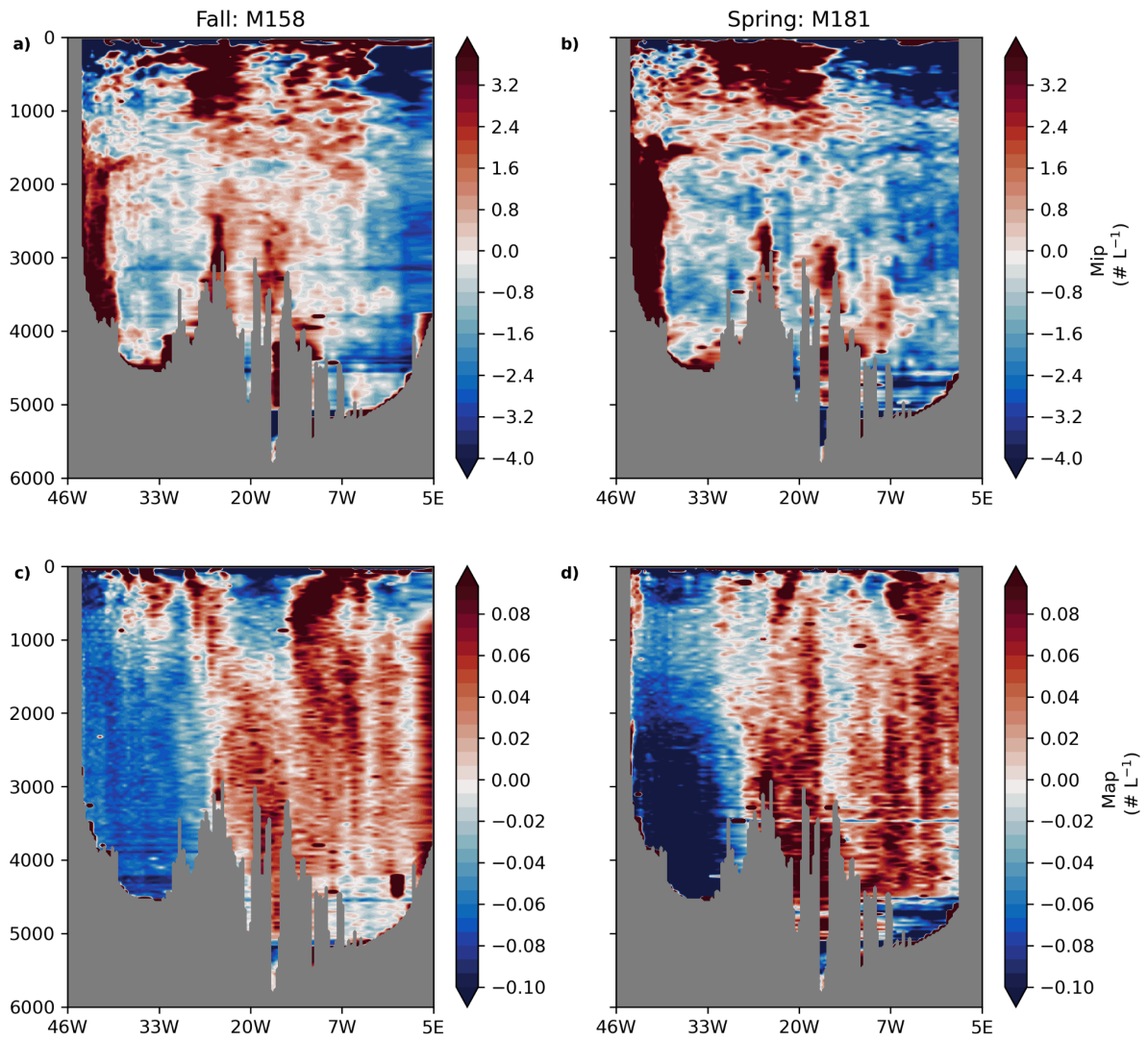

Fig. S6 | Anomalies of MiP, MaP abundance during M158 and M181. (a,b) MiP anomaly (# L^{-1}), (c, d) Map anomaly (# L^{-1}), and (e, f) POC flux anomaly (mg C m^{-2} day^{-1}) measured during the two trans-Atlantic crossings M158 (left panels) and M181 (right panels).

Anomalies were calculated as the deviation of each data point from the mean vertical profile of the full zonal section. Panels show anomalies in micrometric particle (MiP) abundance, macroscopic particle (MaP) abundance, and total particulate organic carbon (POC) flux during fall and spring. The anomaly patterns reveal three distinct export events during M158, located in the eastern, central, and western basins. During M181, a single MiP export event is observed in the western Equatorial Atlantic, while MaP anomalies indicate two export events.

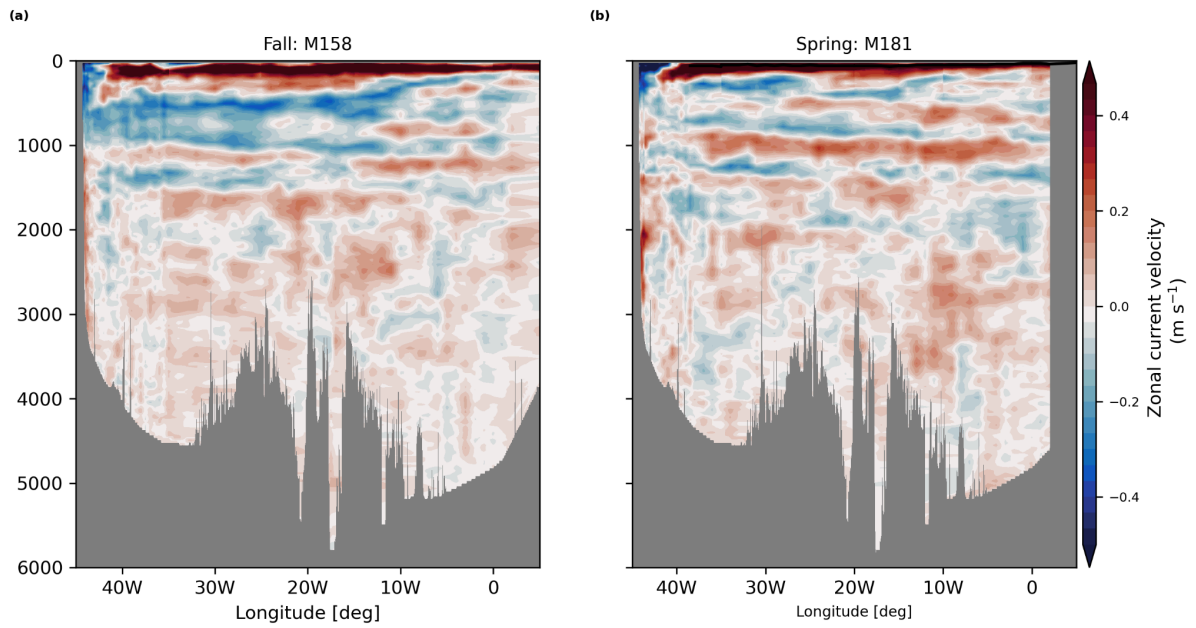

Fig. S7 | Zonal current velocity during M158 and M181. The red color in a, b shows eastward currents.

Deep currents drive the advection of small particles below 1500m in the western region

During both cruises, no MaPs were detected between 30°W and 45°W at depths of 1000–5000 m. However, between 40°W and 45°W, an increase in small particles was observed between 1500 and 4000 m, with evidence of eastward advection associated with the Equatorial Deep Jets. This pattern aligns with the pattern observed on the zonal velocity along the equator (S7) and corresponds to the Deep Western Boundary Current (DWBC) flowing southeastward along the western boundary. This current has two cores: the shallow core is centered at about 1500 m, and a deeper one, at about 3500m (Fisher& schott 1997; Sivkov et al. 2021). This current has been described as bifurcating at the equator into an eastward flow along the equator and a continuous southward flow along the western boundary (Herrfors et al. 2017; McCartney 1994). This layer between 1500-5000m is the noticeable bottom nepheloid layer in the western basin. We suggest that the main reason for its occurrence is the interaction between the DWBC, the shelf, and the Amazon River solid load. The distribution of this reflects primarily the interaction of circulating abyssal waters with the ocean bottom, a strong nepheloid layer that is coincident with western boundary currents. The occurrence of small particles has already been observed in Sivkov et al. 2021; the authors mentioned different bimodal volume-size distributions with particles varying from 2-60 µm.

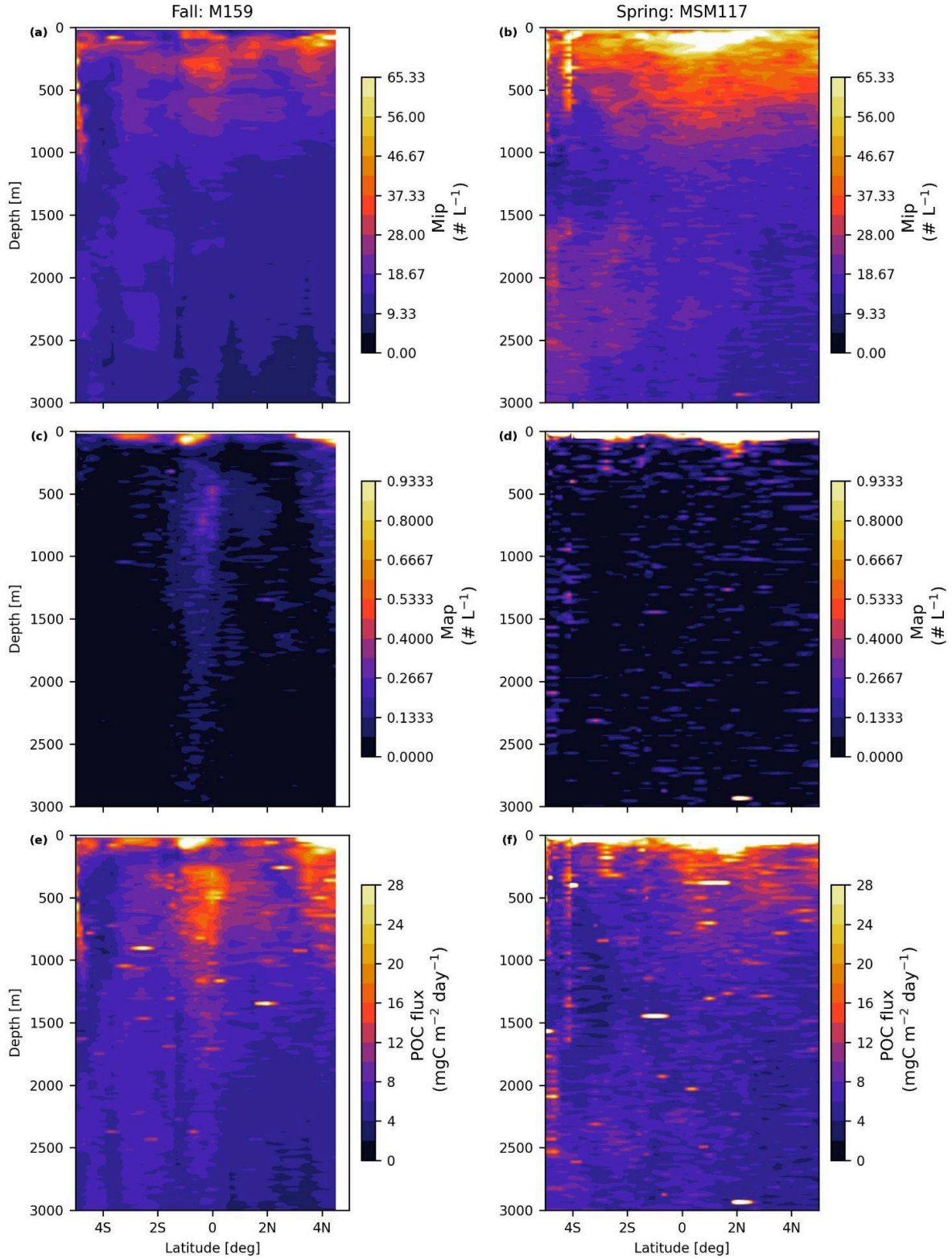

Fig. S8 | Meridional distribution of particle size composition between 5N and 5S. (a,c,e) and (b,d,f) refer to the cruises in fall and spring, respectively. (a,b) MiP abundance (# L^{-1}), (c,d) MaP abundance (# L^{-1}) and, (e,f) POC flux (mgC m^{-2} day^{-1}).

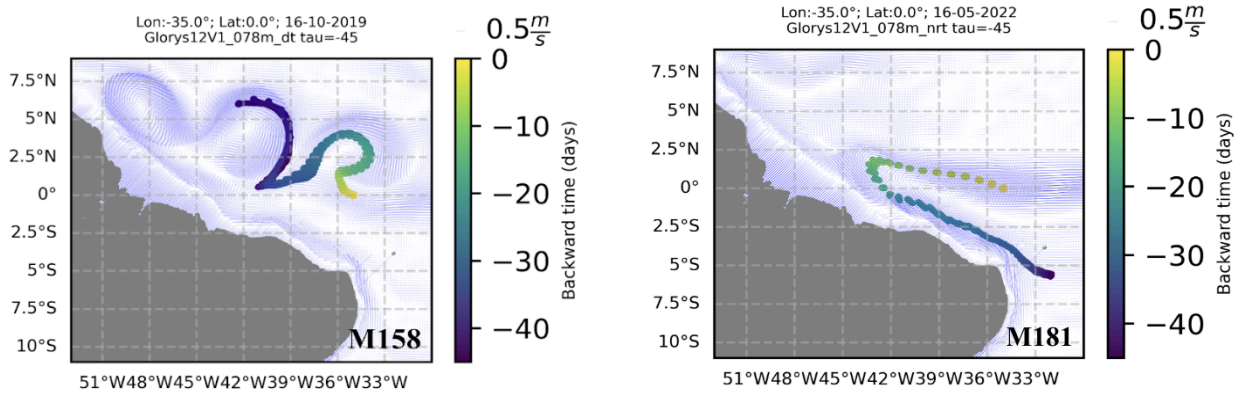

Fig. S9 | Backward Lagrangian particle trajectories for the M158 (left) and M181 (right) campaigns. Particles were released at (0° N, 35° W), at 78 m depth and advected backward in time for 45 days using the GLORYS12V1 velocity field product which has 1/12° spatial resolution and daily temporal resolution. 78m depth was chosen as this depth is considered as representative of the Equatorial Undercurrent (EUC). Particles were advected horizontally using the velocity field at 78 m depth, and their depth was kept constant throughout the simulation. Particles were initially distributed uniformly across the EUC core at the release location, using identical particle density and release configuration for both simulations. Particles were initialised in a circular buffer of 0.1° radius around the release location. Colors indicate backward integration time (days). Light blue arrows show the underlying horizontal velocity field at 78 m depth, with a reference speed of 0.5 m s^{-1}.

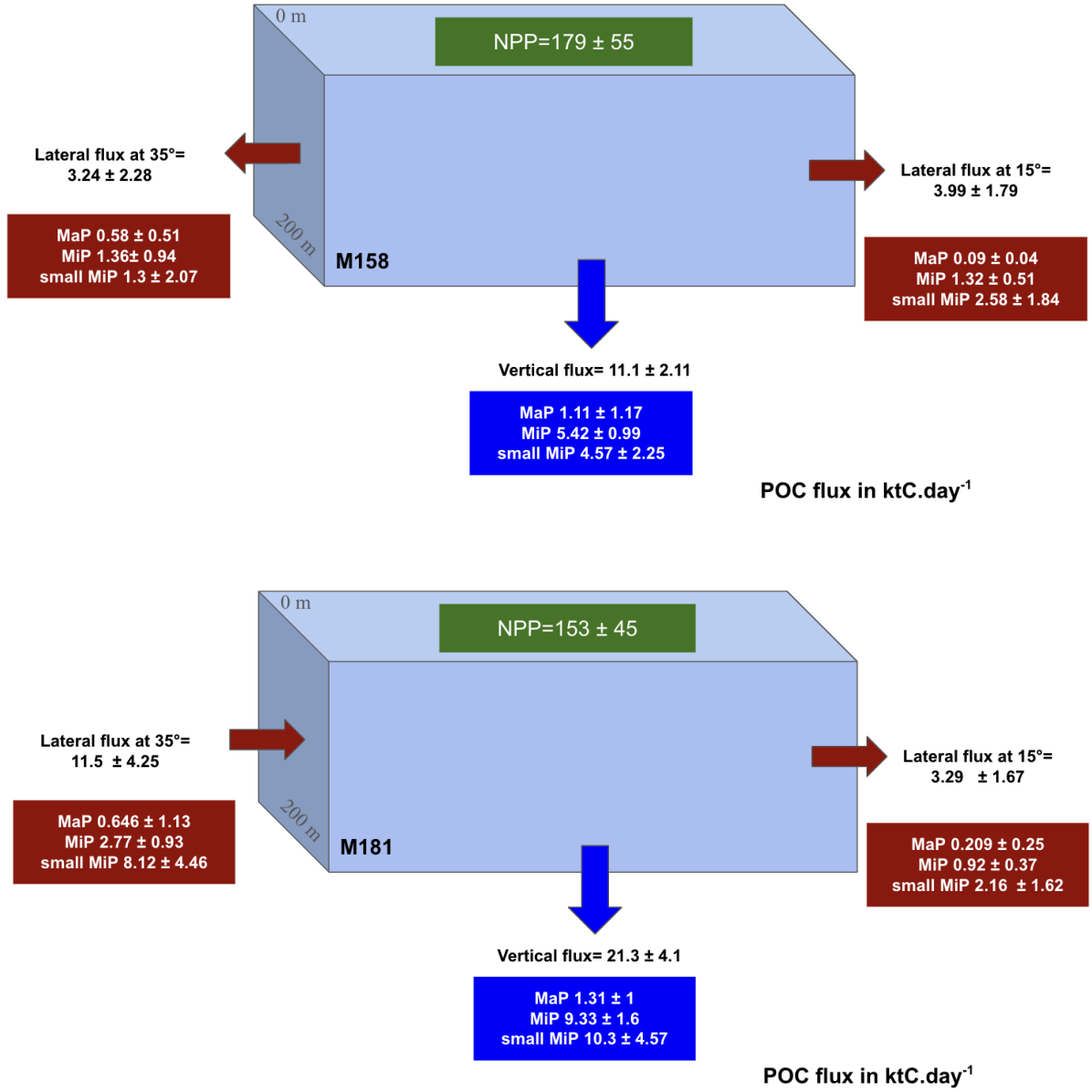

Fig. S10 | Sketch illustrating the calculation of POC supply for M158 and M181. A box of 200 m thickness (Δz) between 15–35°W at the equator and 2° width was used, with 200 m representing the upper boundary of the twilight zone. Sources of organic carbon in this layer include carbon fixation through net primary production (NPP, KtC.day-1) and eastward lateral advection at 35°W, while losses occur via lateral advection at 15°W and downward vertical export of particulate carbon at 200 m. POC flux was calculated separately for three particle groups: MaP (>0.5 mm), MiP (0.102–0.5 mm), and small extrapolated MiP (0.0508–0.102 mm). Excluding the small MiP gives the non-extrapolated flux. The direction of the lateral flux at 35°W differs between cruises, reflecting differences in the depth-averaged (0–200 m) zonal current. During M158, the net flow at 35°W was westward (mean u = −0.14 m/s), indicating that the westward South Equatorial Current dominated over the eastward Equatorial Undercurrent, resulting in a net export of POC out of the box at this boundary. During M181, the depth-mean flow at 35°W was strongly eastward (mean u = +0.5 m s^{-1}), reflecting a stronger EUC, and POC was instead supplied into the box from the west. At 15°W, the flow was eastward during both cruises, consistently exporting POC out of the eastern boundary. This seasonal contrast is visible in the zonal velocity sections (Fig. 3 c,d): during M158, the westward South Equatorial Current near the surface partially compensated the eastward EUC at 35°W, resulting in a net westward depth-averaged flow, whereas during M181 the EUC signal was stronger and shallower, yielding a net eastward flow at this longitude.

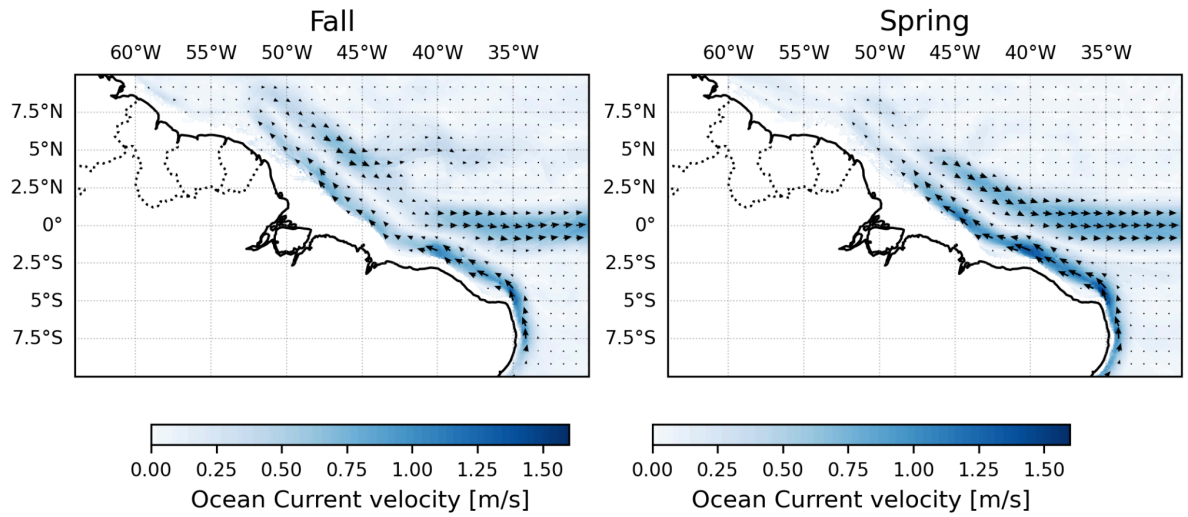

Fig. S11 | Mean circulation of the Equatorial Undercurrent (EUC) during boreal fall (September–November) and spring (April–May), derived from the GLORYS12V1 global ocean physics reanalysis averaged over the period of 2015–2023. Shading indicates mean current speed (m s^{-1}), arrows show the mean velocity field with arrow length proportional to speed. The EUC is defined by potential density layers between 24.5 and 26.3 kg m^{-3}. Similar spatial structures and flow pathways across both seasons, consistent with those observed during our cruises, suggest that the circulation features identified in fall 2019 and spring 2022 are persistent and not confined to the specific periods of the cruise observations.

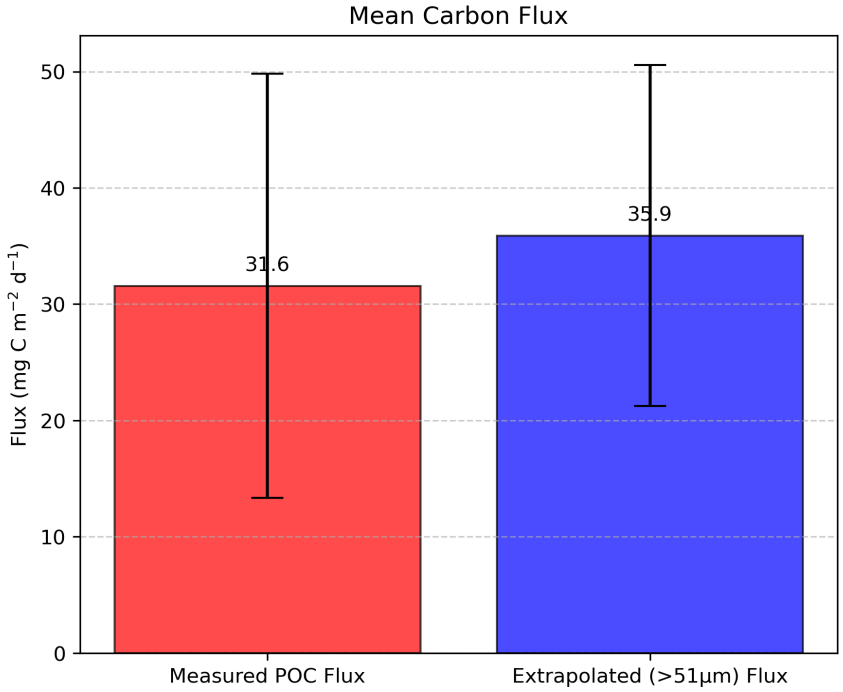

Fig. S12 | Comparison between mean 234Th-derived POC flux (red box) and UVP-based POC flux estimates for particles >51 µm (blue box).